Faraday Discussions

Accepted Manuscript

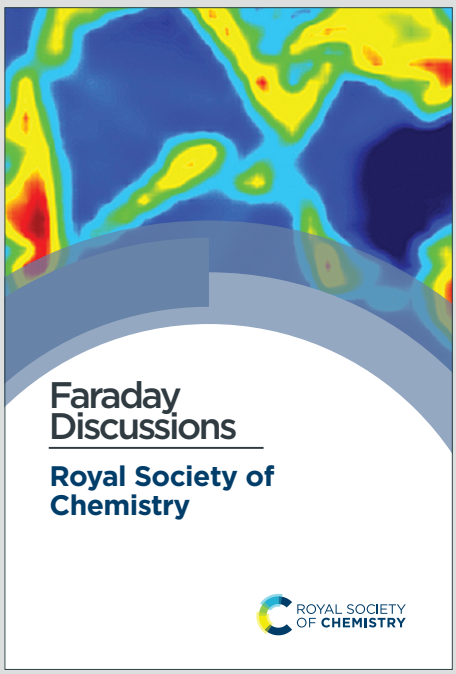

This article can be cited before page numbers have been issued, to do this please use: A. Mangini, G. Zagatti, J. Amici, S. Garcia-Ballesteros and F. Bella, *Faraday Discuss.*, 2026, DOI: 10.1039/D6FD00090H.

ROYAL SOCIETY OF CHEMISTRY

www.rsc.org/faraday_d

Faraday Discussions

View Article Online
DOI: 10.1039/D6FD00090H

PAPER

Electrolyte and gas flow rate balance in flow cell for lithium-mediated ammonia electrosynthesis

Anna Mangini,†[a] Giulia Zagatti,†[a] Julia Amici,[a] Sara Garcia-Ballesteros *[a] and Federico Bella *[a]

[a] Department of Applied Science and Technology, Politecnico di Torino, Corso Duca degli Abruzzi 24, 10129 - Turin, Italy.
† These authors contributed equally to this work / * Corresponding authors: sara.garcia@polito.it; federico.bella@polito.it

Received 00th January 20xx, Accepted 00th January 20xx
DOI: 10.1039/x0xx00000x

Electrochemical lithium-mediated nitrogen reduction (Li-NRR) has emerged as a leading approach for ammonia electrosynthesis under mild conditions, particularly in continuous flow-cell configurations. Despite the rapid progress of this strategy, as well as the remarkable efforts in electrolyte composition engineering and solid electrolyte interphase layer understanding, the impact of archicecture-level parameters remains unclear and is often entangled with the intrinsic process reactivity and selectivity. Here, we systematically investigate the influence of electrolyte and nitrogen gas flow rates on Li-NRR performance in a flow cell, attempting to decouple the effect of device-level parameters from reaction chemistry in determining activity, selectivity, and stability of the system. By balancing liquid and gas flows, we demonstrate stable device operation even at high electrolyte flow rates (18 mL min^{-1}), allowing for a complete exchange of the electrolyte in the liquid chamber twice per minute. This electrolyte flow rate results in a simultaneous improvement of Faradaic efficiency, productivity, and ammonia recovery in the gas phase. Overall, our results highlight the critical influence of cell architecture-related parameters on Li-NRR and emphasize the need to disentangle device engineering from electrolyte tailoring and electrochemical performance optimisation, to enable a rational mechanism understanding, towards the translation of Li-NRR to a scalable process.

Introduction

The electrification of industrial chemical processes has emerged as a central strategy for mitigating climate change and decarbonizing energy-intensive sectors.[1,2] By using renewable electricity to drive electrochemical alternatives to thermally driven operations, these processes can reduce their dependence on fossil-fuel and CO_2 emissions while enabling precise control through electrode potential and flexible operation compatible with intermittent renewable energy.

Within this context, NH_3 synthesis represents a key process due to its global production scale, its pivotal role in the economy, and its dependence on fossil fuels. NH_3 is, indeed, the essential feedstock for the fertilizer industry, which is constantly increasing, driven by the growing global population.[3,4] In parallel, NH_3 is gaining attention as a carbon-free energy carrier and fuel, owing to its high volumetric energy density in comparison with H_2, *i.e.*, 12.9 MJ L^{-1} *vs* 2.76 MJ L^{-1}, and compatibility within existent infrastructure.[5,6] However, a correct evaluation of the technology exploiting this molecule should be carefully done, to keep balanced the nitrogen cycle an minimise the impact of NH_3 production and use.[7,8] Synthetic NH_3 nowadays relies heavily on fossil fuels due to both the high energy intensity of the current process (*i.e.*, the Haber-Bosch process) and to the massive need of H_2 as a reactant. H_2 is indeed primarily produced via steam methane reforming, favoring highly-centralized plants to achieve optimal efficiencies, and thereby limiting compatibility with a low-carbon energy system. As a result, the Haber-Bosch process is responsible for a significant fraction of global CO_2 emissions, accounting for more than 1.4% of the total.[3,9]

Electrochemical routes to NH_3 synthesis have attracted increasing interest as a means to enable new opportunities for sustainable production pathways, *i.e.*, a low-temperature, low-pressure, and decentralized production directly powered by carbon-free energy

View Article Online
DOI: 10.1039/D6FD00090H

sources.[10,9,11] Despite extensive efforts, conventional electrochemical N_2 reduction in aqueous systems has been severely limited by low selectivity arising from the competing H_2 evolution reaction, resulting in poor Faradaic efficiencies (FE) and low NH_3 production rates.[12,13,14]

Among emerging electrochemical processes, the lithium-mediated nitrogen reduction reaction (Li-NRR) has been proven as the most promising strategy under ambient conditions, with reliable and reproducible FE, *i.e.*, up to 64 ± 1% after 300 h operation, opening up to a conceptually feasible scale-up.[15-19] While alternative mediators with lower overpotential and higher reduction potentials than lithium (*i.e.*, −3.04 V *vs* SHE) are being explored to reduce the energetic cost of the process, a critical and complementary challenge lies in understanding and controlling the interfacial chemistry that governs reaction selectivity and stability, and lithium, the behavior of which in organic solvent is well studied in batteries, is the best candidate as the starting point of this technology.[20-23]

In Li-NRR, Li metal is electrochemically deposited from an aprotic electrolyte on the cathode, where it activates N_2 dissolved in the electrolyte or flowed through a gas diffusion electrode (GDE), forming a lithium-nitrogen intermediate. The unique ability of Li to give a stable enough intermediate, but still prone to being protonated into NH_3, enables a quasi-simultaneous reaction of this intermediate with the protons present in the electrolyte, regenerating Li^+ in the electrolyte. Indeed, Li in this process is a mediator rather than a catalyst. The protons used in the reaction should also be continuously supplied to the reactor: in a Li-NRR complete process, the hydrogen oxidation reaction (HOR) or the use of a membrane selective to protons and the coupling with an aqueous compartment may be used.[16,24] In the catholyte, a proton-shuttle molecule is always needed, and ethanol (EtOH) is the most used, as it favors a stable cathodic interface.[25] A defining characteristic of this system is, indeed, the unavoidable formation of a solid electrolyte interphase (SEI) layer on the freshly deposited lithium.[19] The SEI layer takes its name from Li-metal batteries, where extensive studies have established the importance of the SEI layer composition, morphology, and mechanical integrity in regulating interfacial reactivity.[26,27] However, the Li-NRR process presents some different key features, such as the presence of EtOH and the lithium dissolution, which make the system more dynamic than in batteries.[28,29] Owing to the extreme reactivity of Li and the highly negative potential at which the system operates, the electrolyte components undergo reductive decomposition at the cathodic interface, resulting in a heterogeneous, mosaic SEI composed of organic and inorganic species. This interphase plays a rate- and selectivity-regulatory role that is central to Li-NRR performance.[30,28] Other than controlling the transport of Li^+, N_2, and protons to the reactive Li surface, thereby governing activity and selectivity, it also affects long-term stability. Indeed, only when a favorable dynamic equilibrium in the SEI layer composition occurs, it can suppress the electrolyte decomposition at the interface.[15,31] Therefore, tailoring this layer represents a critical challenge, recently addressed by different studies.[32,33,34]

Notwithstanding the promising results obtained at the laboratory scale, the cost and performance with respect to industrial targets, such as the process current density and stability, are still limited.[35] In particular, the stability of the system for long-term operation is still hindered by a comprehensive knowledge of the dynamics of the cathodic interface and its stability. Indeed, the identification of the mechanism leading to the formation of dead Li and passivating species in the SEI layer is still missing, and both of them are architecture-affected.[21,36] Usually, studies regarding the SEI layer characterisation and the cathodic reaction are performed in batch cell, while the flow cell is mostly used for studies are aimed at optimising the full process performances and durability.[37] Rarely the flow cell is used in fundamental studies as *in operando* investigations aimed at characterising the interphase, and the cell architecture is often home-made and may differ from the actual process.[38,39]

In this study, we adapted a commercial flow-cell to the Li-NRR process, and systematically assessed the device parameters, *i.e.*, the gas and electrolyte flow rates, to identify their effect on the cathodic gas-liquid interfacial stability, towards a reproducible design to carry out further investigation of the GDE cathodic interface (***Figure 1***).

View Article Online
DOI: 10.1039/D6FD00090H

In this setup, we achieved stable operation by balancing back pressures and flow rates across the cell compartments, avoiding

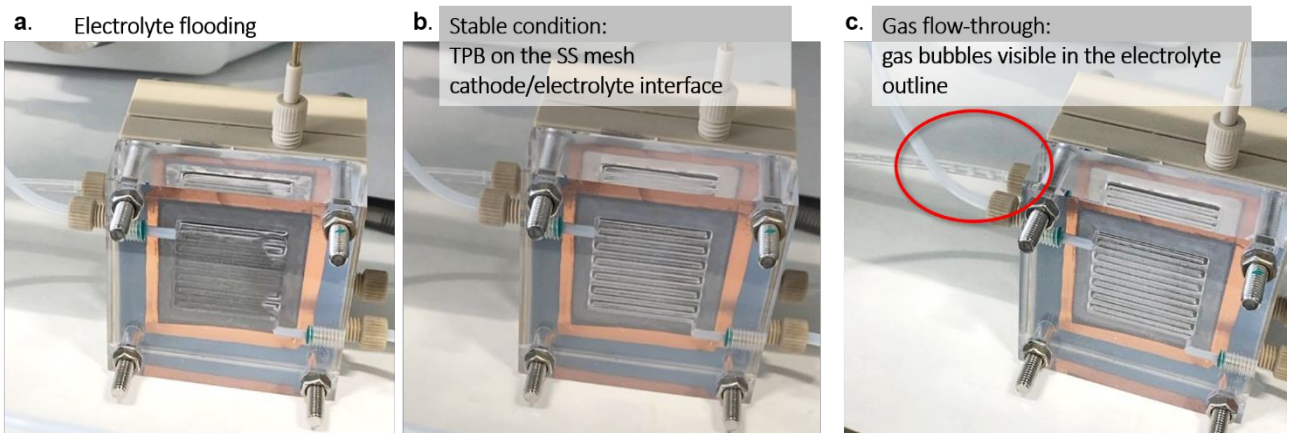

Figure 1: *Photographs of the adapted flow-cell featuring a poly(methyl methacrylate) transparent gas chamber instead of the poly(ether ether ketone) (PEEK) gas chamber used for Li-NRR tests, enabling the tracking of the stainless stell (SS) mesh observation under different flow regimes. The three pictures display the different conditions which may occur at the GDE during operation:* ***a****. electrolyte flooding through the GDE into the gas chamber, and consequent electrolyte outgoing in the gas outline;* ***b.*** *stable condition with a controlled triple-phase boundary (TPB) at the SS mesh cathode/electrolyte interface;* ***c.*** *gas flow-through, identified by gas bubbles in the electrolyte outlet, highlighted by the red circle.*

both flooding (*i.e.*, the passage of the electrolyte through the GDE into the gas chamber) and flow-through conditions (*i.e.*, the passage of gas bubbles through the GDE into the electrolyte chamber). Being the stainless-steel (SS) mesh, used as a cathode, wettable by the organic electrolyte, careful pressure balancing is required to maintain a stable triple-phase boundary (TPB) at the electrode/electrolyte interface.

Moreover, we selected the cell configuration with the aim of disentangling the parameters dependent from the cell architecture to the chemistry-related ones, searching for a preliminary identification of the effect of the different flow rates on the Li deposit and SEI layer formation, N_2 activation and protonation, and targeting NH_3 recovery mainly in the gas phase instead of in the electrolyte.

The application of elevated electrolyte flow rates, in particular when in combination with lower gas stream temperature, emerged as beneficial both for the Li-NRR performance and for the NH_3 recovery in the gas phase, revealing a dependence of the process both on the relative magnitude of gas and electrolyte transport, and in their temperature, and opening to a faster reactants exchange in the system.

Methods

Electrochemical cell: setup, assembly, and testing

Materials and electrode assembly procedure

The SS gauze 325 mesh woven, 0.036 mm Φ wire, type 316 (Thermo Scientific), was cut into 3.5x3.5 cm, cleaned, pre-treated, and assembled on the gasket as described below. The platinum gauze used as anode was the 52 mesh, 99.9% trace metals basis (Sigma-Aldrich); it was cut into 4x4 cm pieces and flame-annealed with a propane torch before each test. A platinum wire (0.2 mm Φ) was twisted around the upper side of the mesh as the current collector.

The SS mesh was pre-treated by washing it with used electrolyte, as this procedure was observed to ensure increased and repeatable performance even re-using the same electrode. Specifically, it was rinsed with ultrapure water, sonicated in acetone (ACS reagent, ≥99.5%, Sigma-Aldrich) in an ultrasonic bath for 5 min at 80 °C, dried and immersed in a post-test electrolyte for 1 h. It was then washed, rinsing with acetone and ultrapure water, and then sonicating 5 min at 80 °C in H_2SO_4 0.001 M, and dried overnight. The same washing procedure was repeated after each test, and an Ar-blank test was performed to ensure the absence of cross-contaminations. A $Li_{0.5}FePO_4$ (LFP) electrode was used as a reference, as previously reported.[25,40,41] To this end, a commercial LFP powder (Aleees) was chemically partially delithiated with $K_2S_2O_8$ (Sigma-Aldrich),[40] mixed with C_{65} (Imerys, Timcal) and poly(vinylidene difluoride) (Arkema) as a binder, in a 70:10:20 ratio, in N-methyl-2-pyrrolidinone (>99.0% Sigma-Aldrich), while maintaining a solid fraction of 20 wt%. The mixture was processed in a ball miller for 5 min at 30 Hz of frequency, using zirconia spheres. The slurry was then deposited by dip coating onto a copper wire (0.5 mm Φ wire, 99.999%, Goodfellow Cambridge Ltd.) previously cleaned with HCl 4 M, rinsed and pre-heated at 60 °C. The electrolyte solution was prepared in a MBraun Ar-filled glovebox (with impurity values: <0.5 ppm H_2O, <0.1 ppm O_2). Lithium tetrafluoroborate (anhydrous, Sigma-Aldrich) was added in

diglyme (DG) (anhydrous, >99.5%, Sigma-Aldrich); when the salt was completely dissolved, and, just before the test was performed, EtOH 0.5 vol% amount was added. For the acid trap, a solution was prepared by diluting HCl 37% (Sigma-Aldrich) up to 0.2 M.

View Article Online
DOI: 10.1039/D6FD00090H

Setup and flow-cell assembly

Tests were conducted in a flow-cell architecture, customized starting from the model CFGD261A1 from DEK research. The cell (***Figure 2***) is composed of: (i) a PEEK gas diffusion chamber featuring a gas flow field of a single-serpentine of 9 cm^2; (ii) two ethylene propylene diene monomer (EPDM) gaskets with a free area of 9 cm^2, in the middle of which the SS mesh is fixed with a conductive copper tape frame then shielded by a electrolyte-compatible, not conductive tape, 0.03 mm-thick, made of poly(ethylene terephthalate) (purchased from MTI); (iii) a PEEK electrolyte chamber 1 cm-thick, with internal volume 9 cm^3, guaranteeing a cross-field flow in respect to the gas flow-field; (iv) two EPDM gaskets with a free area of 16 cm^2, in the middle of which the Pt mesh is positioned; (v) a poly(tetrafluoroethylene) (PTFE) small chamber, internal area 16 cm^2, 2 mm-thick, closed by a PTFE plate. An additional PEEK or SS plate was added to keep the PTFE part flat to guarantee a perfect sealing through the four M6 screws.

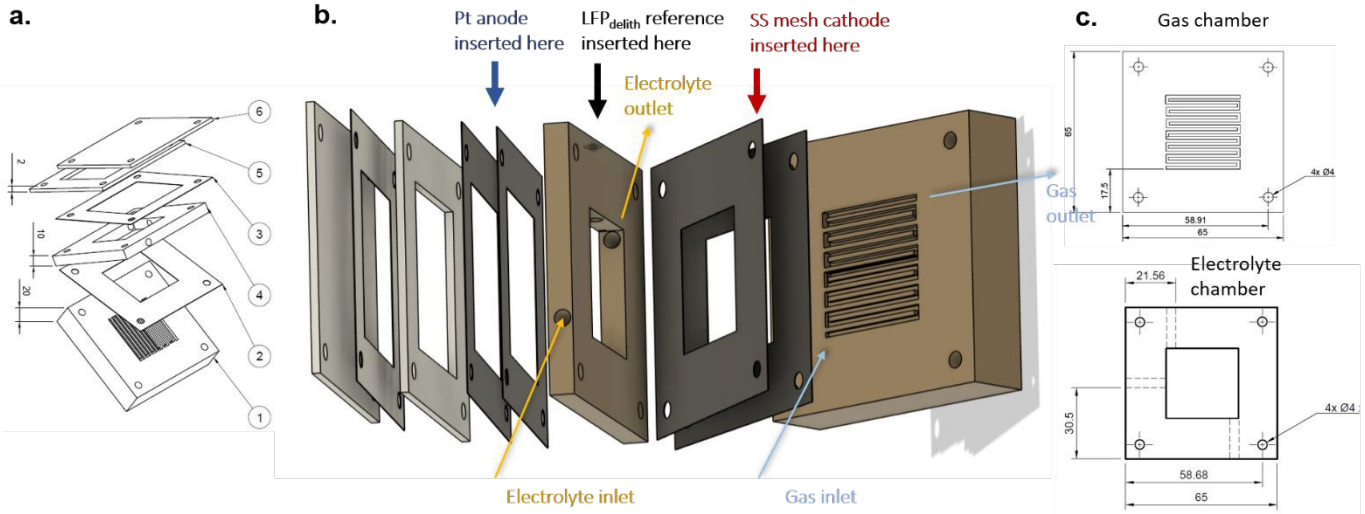

Figure 2*: Customized flow-cell configuration used for Li-NRR experiments.* ***a****. Exploded-view drawn showing the thickness (in mm) of the different components:* ***1****- the PEEK gas chamber featuring a gas flow field of a single-serpentine with a squared active area of 9 cm^2, channel width of 1.4 mm, rib width of 1 mm, channel depth of 1 mm, and a serpentine channel pitch (centre-to-centre distance between adjacent channels) of 2.4 mm;* ***2****- the couple of EPDM gaskets embracing the SS cathode, with a free area of 9 cm^2, thickness 0.8 mm;* ***3****- the couple of EPDM gaskets embracing the Pt anode, with a free area of 16 cm^2, thickness 0.8 mm;* ***4****- the PEEK electrolyte chamber featuring three holes: two of 3.1 mm Φ in the bottom-right and upper-left side of the chamber, used as electrolyte inlet and outlet, respectively, and a third hole in the middle-upper side, of the corner, 4 mm Φ, used to insert the reference electrode through a Si-teflonated septum;* ***5****- the PTFE chamber hosting the Pt anode, 2 mm-thick;* ***6****- the PTFE closing plate.* ***b****. Exploded-view of the adapted assembly, highlighting the position of the SS mesh cathode, Pt gauze anode, and the gas/electrolyte inlet and outlet paths, assembled in a cross-field configuration.* ***c****. Technical drawings of the gas-diffusion flow-field plate and electrolyte chamber, reporting the main geometrical features and dimensions of the customized architecture, in mm.*

To balance the internal pressure in the different chambers, a back pressure was added both in the gas chamber and in the electrolyte one. To establish the desired back-pressure in the gas chamber, an acid trap (40 mL) was installed at the gas outlet, submerging the pipe to a liquid head height of 8.5 cm, corresponding to ~8.5 mbar, in similarity to what was previously reported.[16] In addition, a second acid trap (41 mL) was added to the outlet of a pipe connecting the electrolyte reservoir headspace to equilibrate the back-pressure in the electrolyte chamber, and favour the gas outlet from the gas chamber. The electrolyte reservoir bottle was designed with a fourth entrance, sealed with a septum, enabling the electrolyte (20 mL) insertion and recovery with a syringe, avoiding the solution exposure to air/humidity. A buffer volume was added before both acid traps by adding an intermediate empty-vial trap. These traps were also used to prevent and control the back-diffusion of the acid solution to the cell, and to avoid the electrolyte from passing to the acid whenever flooding occurs. As in the headspace of the electrolyte chamber the gas phase is static in normal conditions, a longer pipe (*ca*. 1 m) was used. For longer experiments, the addition of molecular sieves may be suggested, as well as the use of a pressure controller.

To circulate the electrolyte within the cell, the peristaltic pump Rotarus® flow 50 (Hirschmann) was employed; given the pump material compliance requirement to be combined with electrolyte compatibility, their chemical stability was evaluated *via* swelling tests (***Table S1***). Versilon™ 2001 tubing was initially used, but, as the rigidity was lost after 10 tests, inducing flow variabilities, Chem-Durance® (3.1 mm Φ internal) was selected for this study, as it is internally PTFE-covered. The tubing was connected to the cell inlet and reservoir bottle using perfluoroalkoxy alkanes pipes 3 mm Φ external, inserted and sealed in the Chem-Durance one with PTFE tape. The cell was kept 13 cm higher than the electrolyte reservoir, and the connections were made to avoid the electrolyte pipe from curving towards a higher height.

View Article Online
DOI: 10.1039/D6FD00090H

To control the temperature (T) of gas and electrolyte streams, the electrolyte reservoir was maintained at a constant T *via* a thermostated water bath heating plate, while a band heater was applied to pre-heat a portion of the N_2 gas line downstream of the outside gas cylinder. The reached gas temperature was determined using a thermometer inserted through a septum in an insulated vial or, for the test comparing different temperatures, inserting it directly inside the assembled cell, before the test, using the reference electrode inlet, and flowing N_2 at 27 mL min^{-1} for 1 h in the same environment.
To clean the cell from air internally, after cell assembly and sealing, the whole setup was connected to an Ar stream of 20 mL min^{-1} for 20-30 min. Then, the gas stream was changed to N_2 20 mL min^{-1} for at least 10 min before the electrolyte addition.
After test, the cell was cleaned by rinsing with EtOH or isopropanol, then with distilled water vigorously, then sonicated for 5 min at 80 °C in H_2SO_4 0.001 M, and finally rinsed with ultrapure water. An Ar blank test was performed to verify the effectiveness of this method, using the same setup and procedure as all the other tests of this work, with both gas and electrolyte flow rates of 9 mL min^{-1} (resulting in a FE lower than the FE typical error). Both Ar and N_2 gas (purity 99.9999%) were further purified by passing through commercial filters (Agilent OT3-4).[42]

Test procedure

To set-up the streams, 10 mL min^{-1} was applied for both flows after the back-pressure was connected and the gas was correctly flowing out from the gas-outlet trap, ensuring no leakages were occurring. After the flow balance was verified at those rates, the flow values were changed according to the different test conditions.
For the electrochemical measurements, a SP-150e mono-channel Biologic potentiostat was used. To check the correct assembly and electrical connection of the cell, and to record the value of the internal cell resistance, electrochemical impedance spectroscopy (EIS) was performed between 100 kHz and 0.1 Hz at open-circuit potential. Then, Li-NRR test was performed, applying a galvanostatic constant current density of -6 mA cm^{-2} for 1 min, followed by 1 min of rest and alternating this procedure for 32 times, up to 109 C of total charge passed in the cell, and preceded by 10 current pulses at 25 mA cm^{-2} for 1 s, followed by 5 s of rest; this protocol has been designed in a dedicated study by our team.[43] Just after the test, a second EIS measurement was carried out to check the system reproducibility. The cell was then disconnected, and the SS electrode washing was done to rinse and solve the ensemble of electrodeposited lithium with the SEI layer on it (hereafter referred to as the "deposit"). It was operated by (i) removing and quantifying the electrolyte, (ii) adding 10 mL of DG inside, circulated via the peristaltic pump at a low flow rate (*i.e.*, 5 mL min^{-1}), to minimise the physical removal or detachment of the deposit, and (iii) after DG removal, adding 5 mL of ultrapure water. Simultaneously to the electrolyte removal, 5 mL of the gas-outlet acid trap were sampled, to quantify the NH_3 obtained in the gas phase during the production separately from the one evolved in the gas phase during the electrode washing, related to N-containing intermediates remained un-protonated in the SEI layer.

Analysis

Ions quantification

Ion chromatography (IC) was used to quantify NH_4^+, Li^+, and F^- in the different liquid fractions collected after Li-NRR tests. NH_4^+ was quantified to determine the NH_3 recovered in the electrolyte, acid trap, and cathode-washing solutions. Li^+ and F^- were additionally monitored in the cathode-washing solutions as indicators of electroplated Li and fluorinated salt-derived species remained in the deposits. To this aim, the SS mesh was washed directly inside the cell immediately after the electrochemical tests, as previously explained. The resulting washing solutions were analysed by IC; analyses were performed using an Eco IC system (Metrohm), equipped with a conductivity detector, a Metrohm Suppressor Module (MSM) for anion analysis, and an 863 Compact IC Autosampler. Chromatographic control, data acquisition, and signal processing were carried out using MagIC Net software (Metrohm). For cation analysis, Li^+ and NH_4^+ were separated using a Metrosep C 6 - 250/4.0 cation-exchange column (Metrohm) with direct conductivity detection. A 10 µL injection volume was used. The eluent consisted of 30 mM oxalic acid and HNO_3 0.3 mM, delivered at a flow rate of 0.9 mL min^{-1}. Under these conditions, the background conductivity was approximately 1380 µS cm^{-1}, while the retention times of Li^+ and NH_4^+ were around 5.5 min and 9.5 min, respectively. For anion analysis, F^- was separated using a Metrosep A Supp 19 - 150/4.0 anion-exchange column (Metrohm) coupled to suppressed conductivity detection. Chemical suppression was performed by sequential suppression using an MSM A suppressor module. The eluent consisted of Na_2CO_3 8.0 mM and $NaHCO_3$ 0.25 mM, delivered at a flow rate of 0.8 mL min^{-1}. Under these conditions, F^- eluted at approximately 3.3 min, with a background conductivity of around 20-22 µS cm^{-1} after suppression. More details on the sample preparation procedure, calibration curves, and the corresponding chromatograms are available in supplementary information (***Figure S1***).

Deposit characterisations

Selected electrodes were characterized after the Li-NRR test to assess possible morphological and compositional changes in the deposit induced by different flow operation and temperature conditions. For these analyses, the samples were collected from the cell in the Ar-filled glovebox and a portion of the SS mesh was cut from the upper-left side of the electrode, opposite to the electrolyte outlet line. To reduce the exposure to air, the samples were fixed, with the help of a double-sided adhesive tape, on a

View Article Online
DOI: 10.1039/D6FD00090H

standard stub and mounted on the stage in the glovebox. The stage was then transferred in inert atmosphere to the instrument. The samples were exposed to air only immediately before insertion into the field-emission scanning electron microscopy (FESEM) chamber. FESEM analysis were performed using a Zeiss SUPRA™ 40 microscope equipped with a Gemini column and a Schottky field-emission tungsten tip operated at 1800 K. Images were acquired at 5 kV with a working distance of 2.7-3.6 mm. X-rays diffraction (XRD) was carried out by a PANalytical X'Pert diffractometer equipped with a 2D solid state detector (PIXcel) and a CuKα radiation source. The diffraction profiles were collected from 20 to 80° 2θ, with a step size of 0.03°.

Results and Discussion

Setup design

The first objective of the study was to identify a cell configuration that supports the use of a GDE cathode, thereby minimizing N_2 transport limitations in Li-NRR, while enabling interfacial studies in which chemical effects can be disentangled from architecture-related contributions. To this aim, we selected a GDE-architecture as similar as possible to the batch architecture. The selected setup should minimise the influence of other factors, such as non-uniform Li electrodeposition and the variability associated with HOR as the anodic reaction on the final Li-NRR performance. We therefore decided not to introduce a serpentine in the electrolyte chamber and the H_2 flow and HOR at the anode. Even if this choice prevented the evaluation of long-term stability, and the flow-cell performance may be further maximised with a serpentine, the variability among the performed tests was expected to be reduced in this simplified setup. Specifically, the serpentine affects the pressure gradient and the current distribution, creating a domino effect on the cathode interface homogeneity, undermining reproducible Li electrodeposition. Indeed, Li plating is usually prevented in the cathodic areas facing the serpentine. To guarantee a more homogeneous distribution of the electrolyte flow field in the electrolyte chamber, even without the serpentine, and to minimise possible stagnant regions, high electrolyte flow rates, up to 27 mL min^{-1}, were also evaluated, while the more common values in the Li-NRR literature are around 1-5 mL min^{-1}.[15,16,44] Indeed, preliminary and qualitative flow-field analyses in a simplified 2D domain suggested a decrease of the fluid velocity near the side of the electrolyte chamber, and a preferential fluid path alongside the chamber diagonal (**Figure S2**). The difference in the velocity distribution in the electrolyte chamber appeared more pronounced for low electrolyte flow rates, while from 18 mL min^{-1} a more homogeneous contour plot was observed. The simulations were repeated for 3, 18, and 27 mL min^{-1}, both considering the pure DG as fluid, and conservatively over-estimating the viscosity of the DG - Li salt mixture as from literature data.[45]

To avoid introducing a catalyst for HOR at the anode and the entanglement of its activity and selectivity as an additional parameter, a simpler Pt mesh was selected as the anode, in similarity to batch-cell studies.[46,32] A higher electrolyte or gas flow rate may affect HOR catalyst mechanical stability, selectivity, and fouling, leading to changes in the electrolyte composition among different tests and conditions. As the reaction and deactivation mechanism on the common Au/Pt HOR catalyst remain unclear, the chosen setup is tailored to minimise the number of variables in the system by keeping the anode as simple and constant as possible. The proton consumption and electrolyte oxidation should remain consistent across the different tests. Indeed, even if the stability may be undermined by the electrolyte decomposition and oxidation products, this effect should be similar across the different assessed conditions, disentangling the influence of architecture-related parameters on the cathodic side from their effect on the anode. Even if higher electrolyte flow rates may reduce stagnant regions, as well as the electrolyte contact time with the anodic surface for single passage, the moderate total electrolyte volume cannot guarantee a sufficient dilution of the oxidation product up to a negligible amount in the same way for all the tested conditions.

Therefore, once TPB stability has been achieved at the cathodic interface, and the effect of flow rates on performance and SEI layer composition has been clarified, a future implementation of HOR or of a proton-selective membrane, such as a Pd-based membrane, may be interesting to delve into long-term stability studies of the system.[24] Regarding the effect of an additional H_2 gas stream on the cell stability, as it would have the same back-pressure as the cathodic one and the cell would be symmetrical, it was expected to maintain the same effect and behaviour.

Electrolyte and gas flow rate balancing

Different combinations of gas and electrolyte flow rate (FR_{gas} and FR_{el}, respectively) were assessed, in the range from 3 to 27 mL min^{-1}. The FE was calculated for each combination as process-performance index. As the total charge, electrode area, and time were kept constant among the different tests, the FE is proportional to the NH_3 production rate. The NH_3 recovery in the gas phase is preferred. Therefore, the gas-phase NH_3 fraction, hereafter referred to as $NH_{3\ gas}$, was also assessed for each condition as the amount of NH_3 in the gas-outlet trap relative to the total amount of NH_3 produced, and expressed as a percentage.

Among all possible variable combinations, the tested conditions were selected starting from the most common values in literature, in which low FR_{el} values are combined with high FR_{gas}.[16] The increase of FR_{el} was then targeted with the aim of reducing the presence of stagnant regions in the considerably wide area of the electrolyte chamber. The values of 3, 9, 18, and 27 mL min^{-1} were selected to keep a proportion with the electrolyte chamber volume, *i.e.*, 9 mL. Higher flow rates were considered unnecessary, as higher values, in particular regarding FR_{el}, would increase the pumping system energy consumption and may mechanically affect the stability of the deposit. Moreover, it was observed that, within the present setup, a further increase of

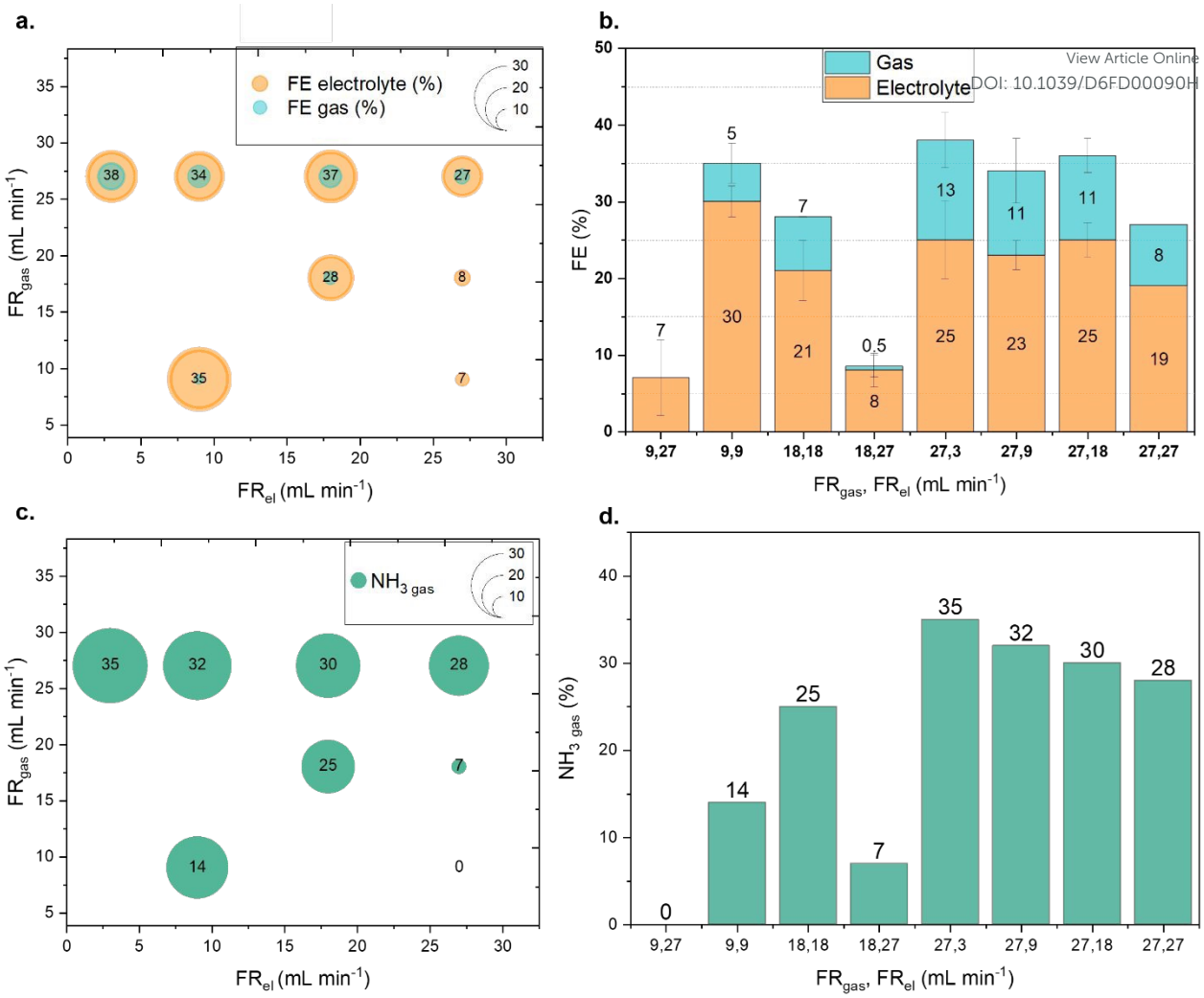

Figure 3: ***a., b.*** *Gas (in light blue) and electrolyte (in orange) FE obtained from Li-NRR tests conducted at 25 °C with different FR_{gas} and FR_{el}; **c., d**. $NH_{3\ gas}$ (in teal) obtained from the respective experiment. In **a**. and **c**., the area of the sphere corresponds to the value of the respective variable (in **a**., in orange for the values corresponding to the electrolyte FE, and in light blue for the FE relative to the NH_3 amount collected from the gas phase; in **c**., the $NH_{3\ gas}$ in teal colour).*

FR_{gas} relative to FR_{el} led to a consistent flow-through phenomenon, preventing a correct Li-NRR test assessment. At first, the higher value (*i.e.*, 27 mL min^{-1}) was set for FR_{gas}, and tested in combination with each possible FR_{el} value. Then, the possibility of combining high FR_{el} with lower FR_{gas} was also tested (right side of the variables perimeter). Subsequently, the combinations of equal values for FR_{gas} and FR_{el} were assessed (the diagonal in the selected space of variables) as the combination of balanced values was suggested from previous results to prevent instability phenomena.

This first set of tests was performed keeping the electrolyte reservoir and gas stream at 25 °C. The most promising FR conditions, selected targeting the maximization of both the total FE and the $NH_{3\ gas}$, and in order to evaluate the system behavior also at high FR_{el}, were then repeated at a slightly lower temperature (*ca*. 17 °C), and the effect of both the gas and electrolyte stream temperatures was deepened. The obtained results are reported in ***Figure 3***. When higher FR_{gas} were applied, as expected, a slight increase of FE and $NH_{3\ gas}$ was registered, while the increase of FR_{el} from 3 to 18 mL min^{-1} at the highest tested FR_{gas} (*i.e.*, 27 mL min^{-1}) was observed not to drastically affect the system, as both the obtained FE and $NH_{3\ gas}$ were similar. The obtained $NH_{3\ gas}$ (*i.e.*, 35%) was lower compared to previous long-term studies,[15] but this result can be ascribed to the shorter test duration and the lower total charge passed, which may prevent full NH_3 saturation of the electrolyte.[38]

At FR_{gas} 27 and FR_{el} 3 or 9 mL min^{-1}, the back-pressure on the electrolyte side was insufficient to prevent gas flow-through, requiring an increase of the liquid column up to ~10.5 cm. When flow-through occurred, the FE increased up to 50%, keeping a similar $NH_{3\ gas}$ distribution. However, it should be taken into consideration that this work aims at identifying a stable condition that ensures reproducibility among different tests, and the flow-through may affect Li deposit unpredictably, drying part of the electrode. Therefore, the results obtained with flow-through were not considered in the data comparison. In these conditions, *i.e.*, with unbalanced gas and electrolyte FR, the TPB is therefore supposed to be more prone to alterations and instability, *e.g.*, whenever accidental alterations in the back-pressures at the electrolyte and gas outlets occur. Moreover, at the lower FR_{el} value, *i.e.*, 3 mL

View Article Online
DOI: 10.1039/D6FD00090H

min^{-1}, more pronounced darkening of the electrolyte was observed, supporting the hypothesis of a significant presence of stagnant regions in the cell, in which an insufficient replenishment of EtOH may lead to a more severe solvent oxidation. However, the registered FE was similar to that obtained at higher FR_{el} and equal FR_{gas}, in which only a slight darkening of the electrolyte was registered at the end of the test. Considering the improved stability of DG in the Li-NRR system in comparison with tetrahydrofuran,[16] and the short test duration, the effect of the electrolyte-oxidation products onto the cathodic interface is supposed to not drastically affect this study. This is supported by the comparison of the FE values obtained in this study with those reported for similar batch setups, with or without HOR.[38,32] The high variability of the FE values obtained for the single point at low FR_{el} is therefore mainly related to the TPB instability and to the more pronounced presence of stagnant regions in the cell, which may lead to a higher degree of inhomogeneity of reactant distribution and electrodeposited lithium and SEI layer formation over the cathodic area.

Flooding was, instead, observed when a FR_{el} as high as 27 mL min^{-1} was combined with lower FR_{gas}, *i.e.*, 18, 9 mL min^{-1}. The back-pressure enhancement was attempted also in this case, but this modification switched the issue to a randomly-appearing flow-through condition, suggesting that the system is in an unstable equilibrium and the TPB may not be guaranteed. The resulting performance registered a drop in the FE, lower than 10%, even if the $NH_{3\ gas}$ was similar. It should be noted that, when flooding occurred, it was mainly observed at the beginning of the test. During the test, the progressive formation of a thicker deposit on the GDE may have prevented the electrolyte crossover through the GDE. When flooding occurred, the flooded electrolyte was removed from the middle empty vial, to avoid trapping of gaseous NH_3 into this liquid fraction from the gas stream, which could otherwise be collected in the acid trap, and falsely counted as $NH_{3\ gas}$. These results suggested that unbalanced FR did not guarantee a correct TPB on the GDE interface.

In the cases where both FR_{gas} and FR_{el} were low but balanced (*i.e.*, both at 9 or 18 mL min^{-1}), the stability was achieved in the device, but the total FE and the $NH_{3\ gas}$ were slightly lower.

The subset of FR conditions identified as more promising, *i.e.*, avoiding visible TPB instability as flooding, and guaranteeing a FE > 30%, was then retested, slightly changing the electrolyte and gas stream temperature to delve into the effect of other setup-related parameters observed to affect the system, *i.e.*, the stream temperatures.

In this case, the gas stream heating was avoided, leaving the gas at the room temperature of *ca.* 17 °C, while the electrolyte reservoir was kept at 20 °C. In this case, both FE and $NH_{3\ gas}$ further increased in comparison with the previous conditions, in particular at high FR_{el}, achieving a $NH_{3\ gas}$ of 37% and a FE of 43 ± 2%, which corresponded, for the proportional ratio previously detailed, to a production rate of 260 ± 12 μg h^{-1} cm$^{-2.43}$ (***Figure 4***).

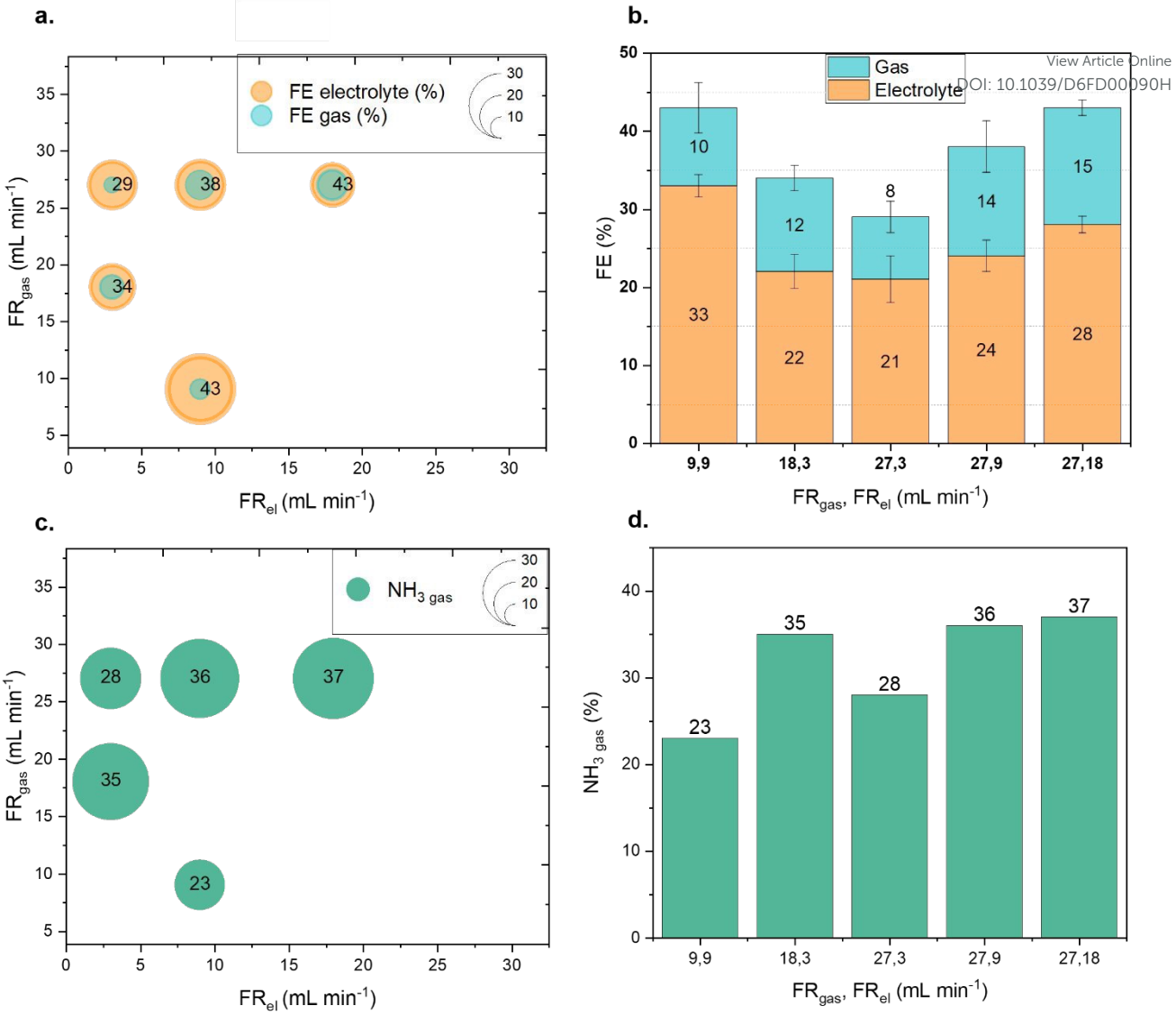

Figure 4: a., b*. Gas (in light blue) and electrolyte (in orange) FE obtained from Li-NRR tests conducted at different FRgas and FRel , and with the electrolyte reservoir bottle at 20 °C. The gas stream was not heated-up in this case, but leaved at the room temperature (ca. 17 °C).* ***c., d****. $NH_{3\ gas}$ (in teal) obtained from the respective experiment. In* ***a****. and* ***c****., the area of the sphere corresponds to the value of the respective variable (in* ***a****., in orange for the values corresponding to the electrolyte FE, and in light blue for the FE relative to the NH_3 amount collected from the gas phase; in* ***c****., the $NH_{3\ gas}$ in teal colour).*

In addition, the variability was lower than that observed at higher temperatures, and again increased at low FR_{el}. As previously mentioned, conditions at low FR_{gas} negatively affected $NH_{3\ gas}$.

FR_{gas} 27 mL min^{-1} and FR_{el} 18 mL min^{-1}, which guaranteed both stability and higher FE and $NH_{3\ gas}$ in all previous tests, were then selected to further investigate the effect of the temperature, a well-known factor impacting the electrodeposited-Li morphology in Li-metal batteries.[47] Specifically, the electrolyte temperature was tested at 20, 25, and 50 °C, as it was previously reported in the batch cell that a slight increase in the electrolyte temperature guaranteed a higher FE, and at lower temperatures a partial crystallization may occur.[46] The gas temperature was instead evaluated from the room temperature up to 30 °C. In one case, the temperature inside the cell was measured before and after the electrolysis, and no changes were registered. This suggests that the possible heat generated by the electrochemical process was negligible compared with the selected temperature differences. As expected, the FE increased when heating up the electrolyte (***Figure 5***), while $NH_{3\ gas}$ remained the same. Conversely, increasing the gas temperature decreased both the FE and $NH_{3\ gas}$, in particular when the gas stream was heated above the electrolyte temperature. As the difference in temperature was studied in a limited range, the effect was assumed to be related to a different deposit and SEI layer nature: a lower temperature in the back of the GDE may favor a different Li electrodeposition, *e.g.,* more porous and gas-permeable, as well as favor a more stable deposit even at higher electrolyte flow rates.[48,49,50]

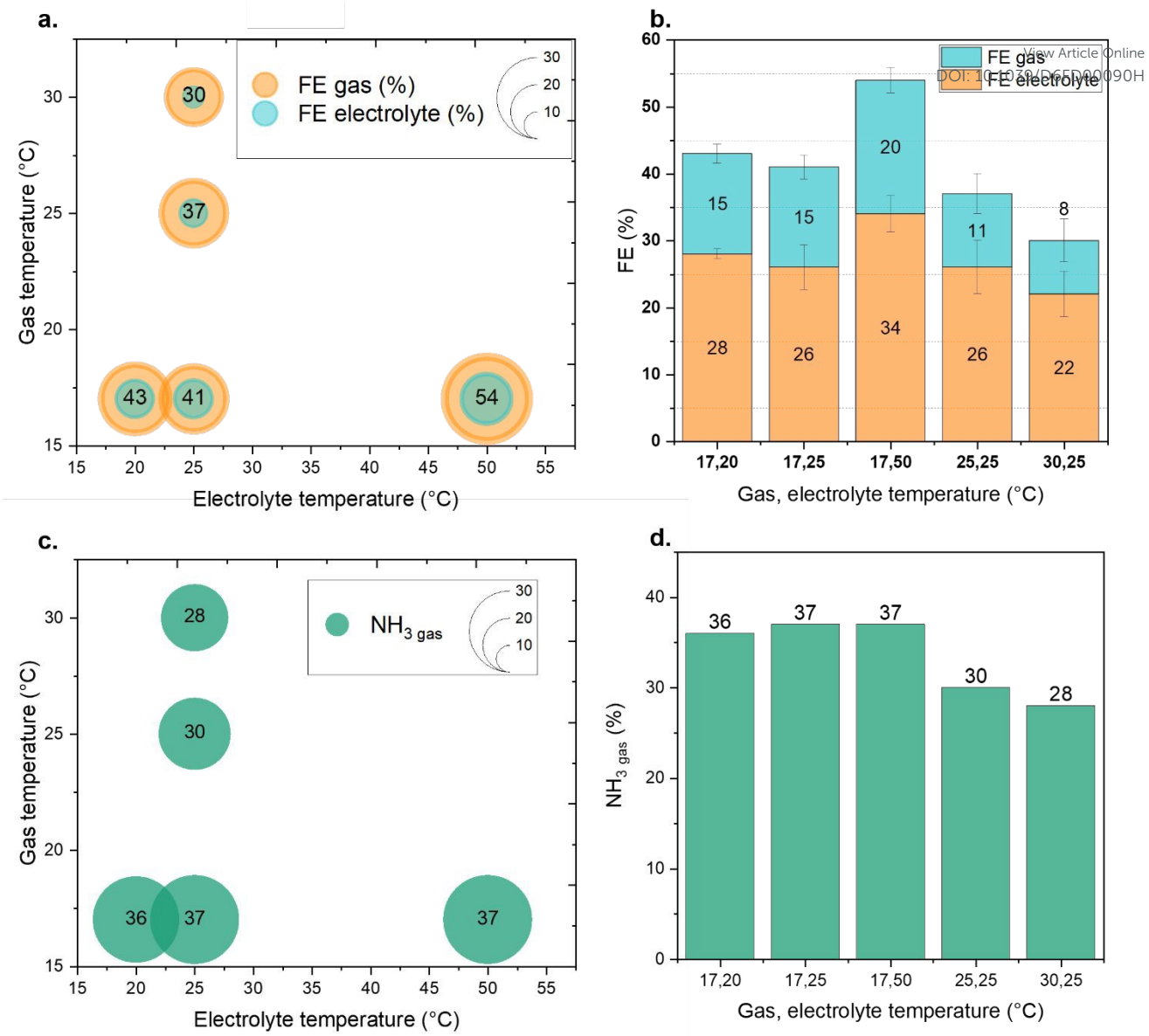

Figure 5: a., b. *Gas (in light blue) and electrolyte (in orange) FE obtained from Li-NRR tests conducted at different gas-stream and electrolyte-reservoir temperature, keeping* FR_{gas} *and* FR_{el} *at 27 and 18 mL* min^{-1}*, respectively.* ***c., d.*** $NH_{3\ gas}$ *(in teal) obtained from the respective experiment. In* ***a.*** *and* ***c.****, the area of the sphere corresponds to the value of the respective variable (in* ***a.****, in orange for the values corresponding to the electrolyte FE, and in light blue for the FE relative to the* NH_3 *amount collected from the gas phase; in* ***c.****, the* $NH_{3\ gas}$ *in teal colour).*

To better investigate the observed trends and their relation with the deposit nature, some of the conditions were then repeated, and after the test the cathode was recovered to perform preliminary characterizations of the deposit formed on it.

Preliminary electrodeposited Li and SEI layer characterisation: interpretation of setup parameters in light of the interfacial changes

The deposits obtained on the SS cathode after the tests in the more promising conditions (*i.e.*, at FR_{gas} 27 mL min^{-1} and FR_{el} at 3, 9, and 18 mL min^{-1}, both at 25 °C and without heating the gas stream) were characterized. The electrodes were washed inside the cell just after the test, to perform Li^+, NH_4^+, and F^- quantification (***Figure 6)***, or were recovered by disassembling the emptied cell in an Ar-filled glovebox for XRD and FESEM analyses. As the hydrolization of both Li and N-intermediates may develop gas (and heat), the acid trap was left connected to the gas-stream outlet to collect eventually evolved NH_3. This NH_3 was then quantified, and its contribution was summed up to the one remaining in the H_2O-washing solution to calculate the FE relative to the unconverted N-intermediates in the deposit. Looking at the quantification results (***Figure 6 a.,d.***), it is possible to observe that the residual Li and F amounts on the cathode were higher when the not-heated gas stream was employed. In this case, part of the deposit was observed to be mechanically detached and was recovered during the first cell wash in DG, as it was possible to distinguish grey particles that came out from the cell in the DG rinsing solution (see the photo in the insert of ***Figure 6 e*****).** This

View Article Online
DOI: 10.1039/D6FD00090H

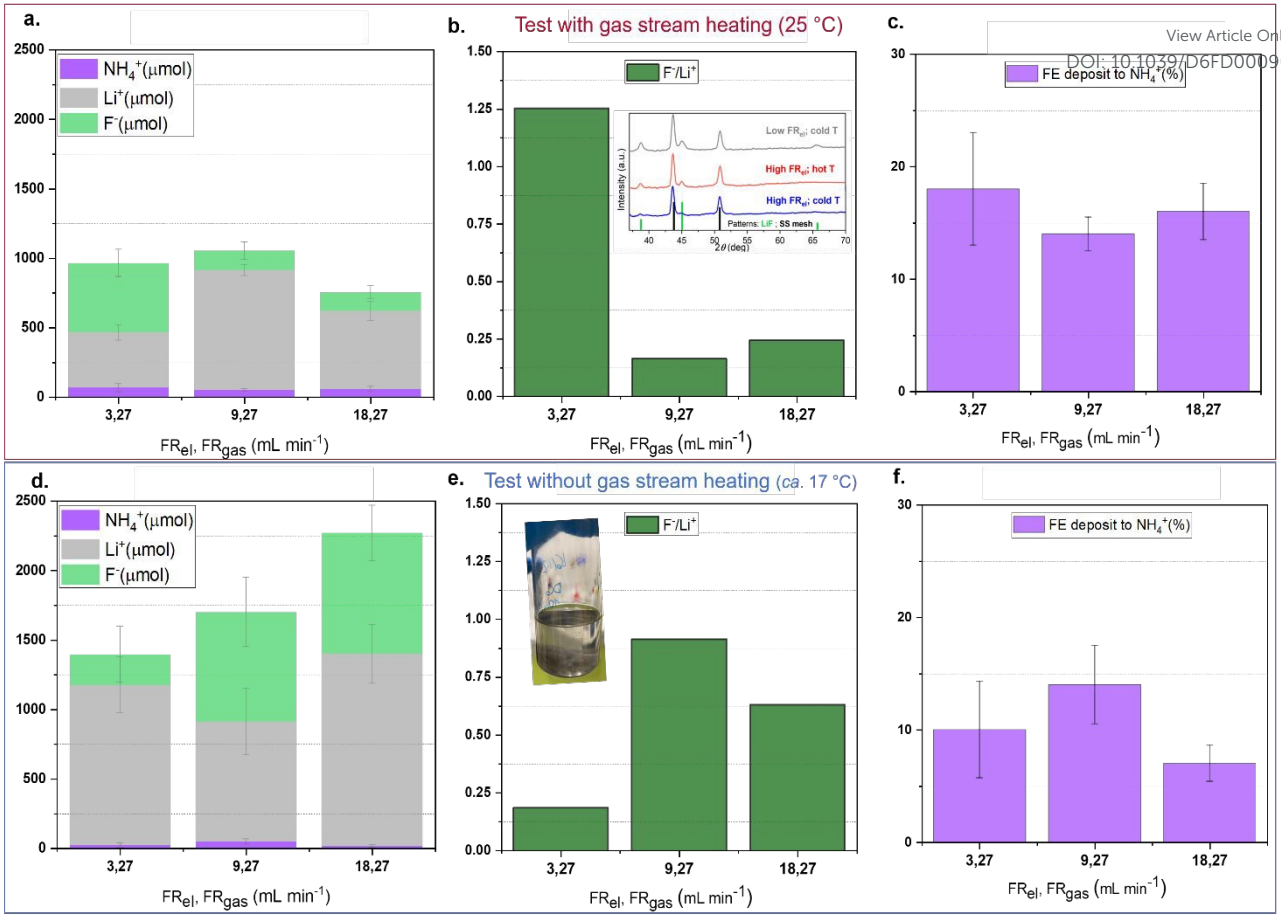

Figure 6: : a., d. *Amount of Li^+, NH_4^+, and F^- obtained from the deposit washing, for the electrodes obtained after Li-NRR test conducted at a FR_{gas} = 27 mL min^{-1} and different FR_{el}, and with the gas stream heated to 25 °C (**a.**) or without gas stream heating, i.e., with the gas stream at room temperature, ca. 17 °C (**d.**) **b., e.** F^- over Li^+ ion ratio, calculated from the quantification reported in **a**. and **d**., respectively. The insert in **b**. shows the XRD patterns of three post-Li-NRR cathodes are reported, with over-imposed the peaks characteristic of LiF (green bars) and of the SS mesh (black bars); specifically, from the top to bottom, the grey line refers to a cathode obtained at a FR_{gas} 27 mL min^{-1} and FR_{el} 3 mL min^{-1}, without heating the gas stream; the red line refers to a cathode obtained at a FR_{gas} 27 mL min^{-1} and FR_{el} 18 mL min^{-1}, heating the gas stream up to 25 °C; the blue line refers to a cathode obtained at a FR_{gas} 27 mL min^{-1} and FR_{el} 18 mL min^{-1}, without heating the gas stream. Insert in **e**. shows a photo of the DG-washing solution as recovered from the cell after a test with the unheated gas stream. **c. f.**, FE obtained from the deposit washing, for the electrodes obtained after Li-NRR test conducted at FR_{gas} 27 mL min^{-1} and different FR_{el}, as specified in the x-axes, and with the gas stream heated to 25 °C (**c.**) or without gas stream heating, i.e., with the gas stream at room temperature, ca. 17 °C (f).*

observation relates to a different deposit morphology obtained at a lower temperature, resulting in a more dendritic and fragile structure, as in batteries.[47,49] This contribution was therefore accounted in the ion quantifications, but subtracted from the medium amount found in DG at higher temperature, which was considered a blank for electrolyte residual washing. However, it should be noted that the presence of salt residues in the cell may not be excluded, not in the DG nor in the distilled water washing solution, as small droplets may remain unseen in the pipes and cell, or part of it may remain onto the deposit, especially when the morphology was more porous. This may therefore also partially explain the higher amount of Li and F registered at lower temperatures.

Looking at the samples collected when heating the gas stream to 25 °C, the amount of Li was slightly lower at FR_{el} of 3 and 18 mL min^{-1}, and again with a marked variability at 3 mL min^{-1}, consistent with the presence of stagnant regions. As the passed charge was the same for the different conditions, the different Li amount registered at 18 mL min^{-1} may relate to a mechanical removal of the deposit from the SS mesh, which would limit the exploitable metal for the NRR process, and is in line with the slightly lower FE registered. Looking at the F^-/Li^+ ratio (***Figure 6 b.,e.***), a higher variability among different FR_{el} was registered at higher temperature, in particular for the low FR_{el}. This ratio is ascribed to the relative amount of LiF in the deposit, a SEI layer component observed in the post-test XRD analysis for all the cathodes (insert in ***Figure 6 b.***). This observation may support the electrolyte degradation enhancement in stagnant regions, leading to inhomogeneity in the cell. The FE obtained from the cathodic wash (***Figure 6 c.,f.***) were slightly higher for the set of tests at higher temperature, in line with a denser deposit, in which the intermediates are less accessible to protons for the complete conversion to NH_3. Among the tests at a colder gas stream, instead,

the lower deposit FE registered for the higher FR_{el} (*i.e.*, 18 mL min^{-1}) may suggest a higher N-intermediate conversion, as it also corresponded to the improved Li-NRR test performance.

View Article Online
DOI: 10.1039/D6FD00090H

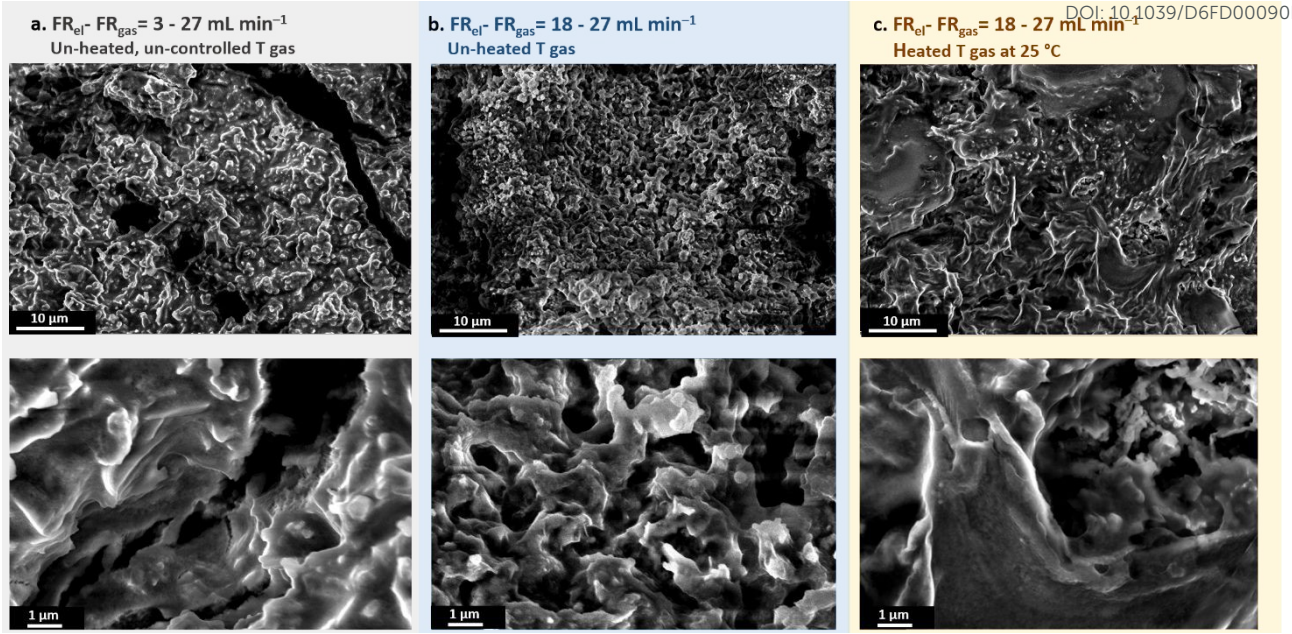

Figure 7: *FESEM micrographs of three post-Li-NRR cathodes obtained at FR_{gas} 27 mL min^{-1}, different FR_{el}, as specified for each panel, with or without the gas stream heated-up at 25 °C.*

The morphology of the deposit was analysed for three selected samples to compare different FR values and gas stream temperatures (***Figure 7***). The samples obtained at a lower gas stream temperature presented an irregular and cracked porous deposit, similar to the one previously reported,[32] and appeared even more porous at higher FR_{el}. This observation is in line with the hypothesis of the formation of a less compact and fragile structure at low gas-stream temperature. The sample obtained at 25 °C showed a moss-like morphology, which may be ascribed to the partial removal of the deposit. In the resulting mosaic structure, the more common particle-like deposit seemed partially covered by an amorphous, gel-like surface layer, supporting the hypothesis of a less porous deposit, but partially depleted in the electrolyte due to the high FR_{el}, and in line with the lower performance registered.

Taken together, these results raise several open questions. For instance, an apparent destabilization of the system, such as the FR_{el} increase, may lead to an improved reactant transport and process performance when balanced by other conditions, in this case the FR_{gas}, back-pressure, and T_{gas}. However, the extent to which this balance can be maintained under long-term operating condition remains to be clarified. On the one hand, the observed effect of a slight variation in the gas stream temperature opens the possibility of tailoring not only the composition, but also the deposit structure to enhance the Li-NRR process performance. On the other hand, the high variability observed in the deposit analyses suggests that a compromise may be required between increasing FR_{el}, which can improve reactant transport and minimize stagnant regions, and avoiding the physical removal of deposited species from the cathode. Indeed, a continuous SEI layer reformation is expected to undermine the FE, although its evolution over time into a potentially passivating interfacial layer is still unclear. Overall, this study further supports the role of the SEI layer as a key dynamic interfacial layer, which prevents the direct transfer of knowledge from aqueous electrolyzer to the Li-NRR system, both in terms of architecture-related parameters and phenomena.

Conclusions

In this work, the influence of gas and electrolyte flow rates on Li-NRR performance was systematically investigated to identify a stable and reproducible operating condition, enabling the standardization of flow-cell architectures.

The flow balancing emerged as a key design parameter for Li-NRR in flow-cell operation. Despite the not negligible variability at individual operating points, a trend of the resultant FE and NH_3 recovery in the gas phase emerged across the explored conditions. An increase of the electrolyte flow rates up to 18 mL min^{-1}, *i.e.*, allowing for the exchange of the electrolyte chamber volume two times per minute, was identified as a favourable operating condition to enable both improved stability and performances.

The results further reveal a strong influence of the temperature of the two flowing streams on the system behaviour. In particular, the gas stream temperature lowering was observed to enhance the NH_3 recovery in the gas phase, and slightly improve the FE, particularly when the high electrolyte flow rate is applied. This effect is supposed to relate to a different Li electrodeposition and SEI layer formation, as observed from preliminary analysis of the deposit remaining on the cathode after the test, and in line with

battery-related studies. Specifically, the combination of low gas stream temperature with high electrolyte flow rate is suggested to enable a less-dense deposit, favouring the reactant exchange and NH_3 gas fraction.

View Article Online
DOI: 10.1039/D6FD00090H

These observations open to future works aimed at widely evaluating and controlling the system temperatures, towards the clarification of the interfacial mechanism underlying the observed trend through further investigations with advanced characterization techniques, such as *in-situ* Raman spectroscopy mapping and *in operando* X-ray synchrotron analysis. More broadly, our findings demonstrate that architecture-related parameters of a flow cell, *i.e.*, the electrolyte and gas flow rates, the related back-pressure balance, and the streams temperature, strongly influence Li-NRR performances and must be carefully controlled and disentangled from the electrochemical activity to enable meaningful comparison between studies.

In conclusion, the proposed GDE-based setup and operating conditions provide a platform for future in-depth investigations of the composition and dynamic evolution of the cathodic interface during Li-NRR in flow cells.

Author contributions

A. Mangini: conceptualization, measurement, data curation, writing – original draft; G. Zagatti: measurement, data curation, formal analysis; J. Amici: measurement, writing – review & editing; S. Garcia-Ballesteros: conceptualization, supervision, writing – review & editing; F. Bella: supervision, funding acquisition, resources, project administration, writing – review & editing.

Conflicts of interest

There are no conflicts to declare.

Data availability

All the data are presented in the manuscript and in the supplementary information. Additional details of IC analysis: polymeric components stability, flow-filed simulation details with relative contour plot, sample preparation procedure, calibration curves, and the corresponding chromatograms are reported in the supplementary information.

Acknowledgements

This project has received funding from the European Research Council (ERC) under the European Union's Horizon 2020 research and innovation program (grant agreement No. 948769, project title: SuN_2rise). The project was also supported by the European Union's Horizon 2020 research and innovation programme under the Marie Skłodowska-Curie grant agreement no. 101107906. This project has received funding from the ERC under the ERC-2024-POC call (grant agreement No. 101213773, project title: GINNY).

Notes and references

1 R. Xia, S. Overa and F. Jiao, *JACS Au*, 2022, **2**, 1054–1070.
2 Z. J. Schiffer and K. Manthiram, *Joule*, 2017, **1**, 10–14.
3 C. Smith, A. K. Hill and L. Torrente-Murciano, *Energy Environ. Sci.*, 2020, **13**, 331–344.
4 US Department of Energy, *U.S. National Clean Hydrogen Strategy and Roadmap*, 2025.
5 W. Shin, H. Lai, G. Ibrahim and G. Zang, *Energy Environ. Sci.*, 2026, **19**, 162–188.
6 G. Jeerh, M. Zhang and S. Tao, *J. Mater. Chem. A*, 2021, **9**, 727–752.
7 M. B. Bertagni, R. H. Socolow, J. M. P. Martirez, E. A. Carter, C. Greig, Y. Ju, T. Lieuwen, M. E. Mueller, S. Sundaresan, R. Wang, M. A. Zondlo and A. Porporato, *PNAS*, 2023, **120**, e2311728120.
8 J. W. Erisman, *One Earth*, 2026, **9**, 1–5.
9 D. R. MacFarlane, P. V. Cherepanov, J. Choi, B. H. R. Suryanto, R. Y. Hodgetts, J. M. Bakker, F. M. Ferrero Vallana and A. N. Simonov, *Joule*, 2020, **4**, 1186–1205.
10 B. Izelaar, M. Ramdin, A. Vlierboom and M. Pe, *Energy Environ. Sci.*, 2024, **17**, 7983–7998.
11 N. S. Morlanés, S. P. Katikaneni, S. N. Paglieri, A. Harale, B. Solami, M. Sarathy and J. Gascon, *Chem. Eng. J.*, 2021, **408**, 127310.
12 E. Skúlason, T. Bligaard, S. Gudmundsdóttir, F. Studt, J. Rossmeisl, F. Abild-Pedersen, T. Vegge, H. Jónsson and J. K. Nørskov, *Phys. Chem. Chem. Phys.*, 2012, **14**, 1235–1245.
13 S. Z. Andersen, V. Čolić, S. Yang, J. A. Schwalbe, A. C. Nielander, J. M. McEnaney, K. Enemark-Rasmussen, J. G. Baker, A. R. Singh, B. A. Rohr, M. J. Statt, S. J. Blair, S. Mezzavilla, J. Kibsgaard, P. C. K. Vesborg, M. Cargnello, S. F. Bent, T. F. Jaramillo, I. E. L. Stephens, J. K. Nørskov and I. Chorkendorff, *Nature*, 2019, **570**, 504–508.

14 J. H. Montoya, C. Tsai, A. Vojvodic and J. K. Nørskov, *ChemSusChem*, 2015, **8**, 2180–2186.
15 S. Li, Y. Zhou, X. Fu, J. B. Pedersen, M. Saccoccio, S. Z. Andersen, K. Enemark-Rasmussen, P. J. Kempen, C. D. Damsgaard, A. Xu, R. Sažinas, J. B. V. Mygind, N. H. Deissler, J. Kibsgaard, P. C. K. Vesborg, J. K. Nørskov and I. Chorkendorff, *Nature*, DOI:10.1038/s41586-024-07276-5.
16 X. Fu, J. B. Pedersen, Y. Zhou, M. Saccoccio, S. Li, R. Sažinas, K. Li, S. Z. Andersen, A. Xu, N. H. Deissler, J. B. Valbæk Mygind, C. Wei, J. Kibsgaard, P. C. K. Vesborg, J. K. Nørskov, I. Chorkendorff, B. J. V. Mygind and C. Wei, *Science (80-.).*, 2023, **379**, 707–712.
17 H. Iriawan, A. Herzog, S. Yu, N. Ceribelli and Y. Shao-Horn, *ACS Energy Lett.*, 2024, **9**, 4883–4891.
18 B. H. R. Suryanto, K. Matuszek, J. Choi, R. Y. Hodgetts, H. L. Du, J. M. Bakker, C. S. M. Kang, P. V. Cherepanov, A. N. Simonov and D. R. MacFarlane, *Science (80-.).*, 2021, **372**, 1187–1191.
19 A. Mangini, L. Fagiolari, A. Sacchetti, A. Garbujo, P. Biasi and F. Bella, *Adv. Energy Mater.*, 2024, **14**, 2400076.
20 R. Tort, A. Bagger, O. Westhead, Y. Kondo, A. Khobnya, A. Winiwarter, B. J. V. Davies, A. Walsh, Y. Katayama, Y. Yamada, M. P. Ryan, M. M. Titirici and I. E. L. Stephens, *ACS Catal.*, 2023, **13**, 14513–14522.
21 X. Ding, Z. Wen and X. Fu, *One Earth*, 2026, **9**, 1–20.
22 C. K. Klein and K. Manthiram, *Joule*, 2022, **6**, 1969–1980.
23 J. B. Goodenough and Y. Kim, *Chem. Mater.*, 2010, **22**, 587–603.
24 B. Ye, C. Burdis, V. Mints, Y. Zhou, A. Khobnya, G. Chen, R. Tort, J. Rietbrock, A. Kafizas, M. P. Ryan, M. M. Titirici and I. E. L. Stephens, *ACS Energy Lett.*, 2026, **11**, 1907–1915.
25 J. B. V. Mygind, J. B. Pedersen, K. Li, N. H. Deissler, M. Saccoccio, X. Fu, S. Li, R. Sažinas, S. Z. Andersen, K. Enemark-Rasmussen, P. C. K. Vesborg, J. Doganli-Kibsgaard and I. Chorkendorff, *ChemSusChem*, 2023, **16**, e202301011.
26 E. Peled, *J. Electrochem. Soc.*, 1979, **126**, 2047.
27 S. K. Heiskanen, J. Kim and B. L. Lucht, 2019, 2322–2333.
28 N. Lazouski, K. J. Steinberg, M. L. Gala, D. Krishnamurthy, V. Viswanathan and K. Manthiram, *ACS Catal.*, 2022, **12**, 5197–5208.
29 K. Steinberg, X. Yuan, N. Lazouski, C. K. Klein, K. Manthiram and Y. Li, *Nat. Energy*, 2023, **8**, 138–148.
30 S. Z. Andersen, M. J. Statt, V. J. Bukas, S. G. Shapel, J. B. Pedersen, K. Krempl, M. Saccoccio, D. Chakraborty, J. Kibsgaard, P. C. K. Vesborg, J. Nørskov and I. Chorkendorff, *Energy Environ. Sci.*, 2020, **13**, 4291–4300.
31 S. Li, Y. Zhou, K. Li, M. Saccoccio, R. Sažinas, S. Z. Andersen, J. B. Pedersen, X. Fu, V. Shadravan, D. Chakraborty, J. Kibsgaard, P. C. K. Vesborg, J. K. Nørskov and I. Chorkendorff, *Joule*, 2022, **6**, 2083–2101.
32 A. Mangini, J. B. V. Mygind, S. Garcia Ballesteros, A. Pedico, M. Armandi and F. Bella, *Angew. Chem. Int. Ed.*, 2025, **64**, e202416027.
33 N. H. Deissler, J. B. V. Mygind, K. Li, V. A. Niemann, P. Benedek, V. Vinci, S. Li, X. Fu, P. C. K. Vesborg, T. F. Jaramillo, J. Kibsgaard, J. Drnec and I. Chorkendorff, *Energy Environ. Sci.*, 2024, **17**, 3482–3492.
34 M. Spry, J. Rietbrock, O. Westhead, C. Burdis, C. Tseng, A. Morinaga, J. O. Douglas, M. S. Conroy, Y. Kondo, Y. Yamada, M. M. Titirici, I. E. L. Stephens and Y. Katayama, *Energy Environ. Sci.*, DOI:10.1039/d5ee01961c.
35 N. Lazouski, A. Limaye, A. Bose, M. L. Gala, K. Manthiram and D. S. Mallapragada, *ACS Energy Lett.*, 2022, **7**, 2627–2633.
36 O. Westhead, R. Tort, J. O. Douglas, M. Conroy, B. J. V. Davies, A. Winiwarter, A. Faisal, M. Spry, A. Khobnya, M. P. Ryan, M.-M. Titirici, R. Jervis and I. E. L. Stephens, *ChemRxiv*, DOI:10.1021/jacs.5c03389.
37 C. Burdis, S. Zamany Andersen, J. Barrio, M. Titirici, I. E. L. Stephens and M. Saccoccio, *Curr. Opin. Green Sustain. Chem.*, 2024, **50**, 100964.
38 N. H. . Deissler, J. B. V. . Mygind, V. A. . Niemann, J. B. Pedersen, V. Vinci, S. Li, X. Fu, T. F. Jaramillo and J. Kibsgaard, *Energy Environ. Sci.*, 2026, **19**, 849.
39 N. H. Deissler, V. Vinci, J. Bjarke, V. Mygind, X. Fu, S. Li, J. Kibsgaard, J. Drnec and I. Chorkendorff, *Next Energy*, 2025, **8**, 100279.
40 E. J. Mcshane, P. Benedek, V. A. Niemann, S. J. Blair, G. A. Kamat, A. C. Nielander, T. F. Jaramillo and M. Cargnello, *ACS Energy Lett.*, 2023, **8**, 230–235.
41 R. Tort, O. Westhead, M. Spry, B. J. V. Davies, M. P. Ryan, M. M. Titirici and I. E. L. Stephens, *ACS Energy Lett.*, 2023, **8**, 1003–1009.
42 B. Izelaar, D. Ripepi, D. D. van Noordenne, P. Jungbacker, R. Kortlever and F. M. Mulder, *ACS Energy Lett.*, 2023, **8**, 3614–3620.
43 Mangini A. et al., under review.
44 X. Fu, S. Li, N. H. Deissler, J. B. V. Mygind, J. Kibsgaard and I. Chorkendorff, *ACS Energy Lett.*, 2024, **9**, 3790–3795.
45 I. Geoffroy, P. Willmann, K. Mesfar, B. Carre and D. Lemordant, *Electrochim. Acta*, 2000, **45**, 2019–2027.
46 P. Benedek, Y. E. . Cornejo-Carrillo, A. H. . O'Rafferty, V. A. . Niemann, S.-W. Lee, E. J. . McShane, M. Cargnello, A. C. . Nielander and T. F. Jaramillo, *Joule*, 2025, **9**, 101810.
47 M. Jeong and K. B. Hatzell, *Phys. Rev. Appl.*, 2024, **10**, 1.
48 S. Weng, X. Zhang, G. Yang, S. Zhang, B. Ma, Q. Liu, Y. Liu, C. Peng, H. Chen, H. Yu, X. Fan, T. Cheng, L. Chen, Y. Li, Z. Wang and X. Wang, 2023, 1–11.
49 X. Gao, Y. Zhou, D. Han, J. Zhou, D. Zhou, W. Tang and J. B. Goodenough, 2020, 1864–1879.
50 G. Tang, L. Men, Y. Wang, R. Xu and Y. Peng, *Nano Lett.*, 2025, **25**, 2561–2567.

[a] *Department of Applied Science and Technology, Politecnico di Torino, Corso Duca degli Abruzzi 24, 10129 - Turin, Italy.*
† These authors contributed equally to this work

View Article Online
DOI: 10.1039/D6FD00090H

Data availability

All the data are presented in the manuscript and in the supplementary information. In the supplementary information are reported additional details of IC analysis: sample preparation procedure, calibration curves and the corresponding chromatograms.